THE JOURNAL OF PHYSICAL CHEMISTRY C

Article

pubs.acs.org/JPCC

$NiFe_2O_4$ Nanoparticles Catalytic Effects of Improving $LiAlH_4$ Dehydrogenation Properties

Ping Li,[†] Ziliang Li,[†] Fuqiang Zhai,[‡] Qi Wan,[†] Xingquan Li,[†] Xuanhui Qu,*[,†] and Alex A. Volinsky[§]

[†]Institute for Advanced Materials and Technology, University of Science and Technology Beijing, 30 Xueyuan Road, Haidian, Beijing 100083, China

[‡]Departament Física Aplicada, EETAC, Universitat Politècnica de Catalunya- BarcelonaTech, Esteve Terradas, 7, 08860 Castelldefels, Spain

[§]Department of Mechanical Engineering, University of South Florida, 4202 East Fowler Avenue, ENB 118, Tampa, Florida 33620, United States

Supporting Information

ABSTRACT: The effects of $NiFe_2O_4$ nanoparticles addition on the dehydrogenation behavior of $LiAlH_4$ were investigated. The onset dehydrogenation temperature for $LiAlH_4$+3 mol % $NiFe_2O_4$ sample is 61 °C, which decreased by 94 °C compared with the as-received $LiAlH_4$ and released ~7.2 wt % hydrogen when heated to 180 °C. Isothermal desorption measurements show that the 3 mol % $NiFe_2O_4$-doped sample releases ~7.0 wt % of hydrogen in 91 min at 120 °C, which is 6.3 wt % higher than the as-received $LiAlH_4$ under the same conditions. Through calculating the apparent activation energy of the $LiAlH_4$ samples with and without $NiFe_2O_4$ for the first two dehydrogenation stages, the E_a of the $LiAlH_4$+3 mol % $NiFe_2O_4$ sample is 54.3 and 70.8 kJ/mol, resulting in 52.5 and 59% decrease, respectively, compared with the as-received $LiAlH_4$. Analyzing the X-ray diffraction and Fourier transform infrared spectroscopy results, it is reasonable to believe that the remarkable improvement of dehydrogenation properties of $NiFe_2O_4$-doped $LiAlH_4$ results from the in situ formed $LiFeO_2$ and Al−Ni compounds, providing the active sites for nucleation and growth of the dehydrogenation products.

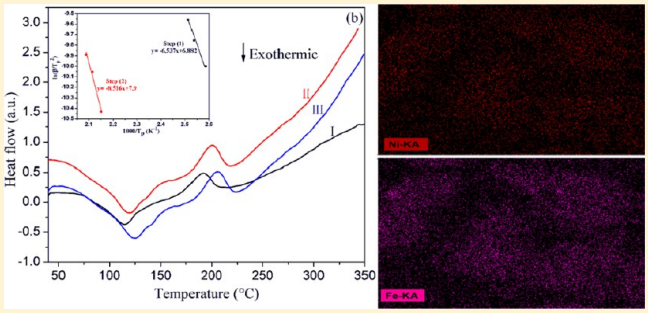

1. INTRODUCTION

Currently, there are multiple efforts focusing on researching complex hydrides as a promising environmentally friendly energy carrier candidate due to their high volumetric and gravimetric hydrogen-storage capacity. However, their relatively high desorption temperature and poor desorption kinetics have become the major obstacles for practical applications.[1,2] Since the de/rehydrogenation performance of $NaAlH_4$ ameliorated by $TiCl_3$ doping was reported,[3] there is a great deal of work enhancing the de/rehydrogenation properties of Alanate-based complex metal hydrides by doping them with various catalysts. Because of the relatively low dehydrogenation temperature and larger theoretical hydrogen desorption content, close to 10.6 wt %, $LiAlH_4$ has become the leader among the large variety of alanates, not only for the fundamental research of absorption and desorption mechanisms but also for technological applications.[4,5] The dehydrogenation of $LiAlH_4$ occurs upon heating according to the following three reactions R1−R3,[6] respectively:

$$3LiAlH_4 \rightarrow Li_3AlH_6 + 2Al + 3H_2\ (150 - 175\ ^\circ C,\ \text{desorbing 5.3 wt \% } H_2) \quad (R1)$$

$$Li_3AlH_6 \rightarrow 3LiH + Al + 3/2H_2\ (180 - 220\ ^\circ C,\ \text{desorbing 2.6 wt \% } H_2) \quad (R2)$$

$$3LiH + 3Al \rightarrow 3LiAl + 3/2H_2\ (400 - 420\ ^\circ C,\ \text{desorbing 2.6 wt \% } H_2) \quad (R3)$$

It is common that only the first two dehydrogenation processes of $LiAlH_4$ are considered due to the fact that the reaction R3 cannot meet the practical application requirements based on not only the onset decomposition temperature above 400 °C but also releasing merely 2.6 wt % of H_2. Hence, in this work it is reasonable to consider only the first two dehydrogenation steps of $LiAlH_4$.

Lithium alanate hydride ($LiAlH_4$) indeed has superior intrinsic hydrogen storage capacity. Nevertheless, many efforts have been devoted to solve the crucial $LiAlH_4$ drawbacks for practical applications, corresponding to high thermodynamic stability and slow desorption kinetics by doping various catalysts. To date, the documented catalysts for $LiAlH_4$ fall

Received: August 21, 2013
Revised: November 14, 2013
Published: November 19, 2013

into six categories: (1) elemental metal, such as Ni,[7,8] Fe,[7,9,10] V,[7,14] Sc,[14] and Ti;[7,10−14] (2) alloy, such as Al_3Ti, Ti_3Al, Al_3Fe and $Al_{22}Fe_3Ti_8$;[10] (3) carbon material, such as CNFs,[15] TiC,[16] and carbon black;[7] (4) halide, such as $AlCl_3$,[7] $FeCl_3$,[7] $TiCl_3$·1/3$AlCl_3$,[11,17] VBr_3,[18] VCl_3,[18] $HfCl_4$,[19] $ZrCl_4$,[19] $LaCl_3$,[20] $TiCl_3$,[21] $ZnCl_2$,[21] $NiCl_2$,[22] TiF_3,[23] NbF_5,[24] $MnCl_2$,[25] K_2TiF_6,[26] $TiCl_4$,[27] and NH_4Cl;[28] (5) metallic oxides, such as TiO_2,[29] Nb_2O_5,[30] Cr_2O_3,[30] $MnFe_2O_4$,[31] Fe_2O_3,[32] and Co_2O_3;[32] (6) and others, such as nanosized TiH_2,[33] $Ce(SO_4)_2$,[34] VCl_3 and CNFs,[15] SWCNT-metallic,[35] and TiN.[4] Most of these catalysts do not work with $LiAlH_4$ as a suitable hydrogen-storage medium. Therefore, persistent efforts are needed to find new efficient catalysts for improving $LiAlH_4$ hydrogen storage.

Transition metals have multivalent states, forming various metal oxides, which have been proven to possess superior catalytic efficiency. Sun et al.[22] reported that the dehydrogenation performance of $LiAlH_4$ was dramatically improved by doping $NiCl_2$, resulting from $NiCl_2$ forming the in situ active Ni species. Recently, Fe species with varying valence have been demonstrated to provide favorable effects on improving $LiAlH_4$ dehydrogenation properties.[31,32] Therefore, combining the above two positive considerations, it is reasonable to illustrate that Ni ferrite ($NiFe_2O_4$) as the catalyst for $LiAlH_4$ shows a great potential to significantly enhance the de/rehydrogenation performance of $LiAlH_4$.

In the present work, the catalytic effects of adding $NiFe_2O_4$ nanopowder as a catalyst precursor on the de/rehydrogenation behavior were investigated. To further understand the catalytic mechanism on $LiAlH_4$, the powder morphology variation and the phase transition was observed and tested by scanning electronic microscopy (SEM), transform infrared spectroscopy (FTIR), and X-ray diffraction (XRD), respectively.

2. EXPERIMENTAL SECTION

2.1. Preparation. The ball-milling process of $LiAlH_4$ (≥95% pure, Sigma Aldrich) and $NiFe_2O_4$ nanoparticles (≥99.99% pure, 20 nm) was conducted in a high-energy Spex mill (QM-3B) for 30 min with a 1200 rpm rotation rate. After every 10 min of milling, a 5 min delay was introduced for cooling the samples. Samples handling was conducted in a glovebox with a high-purity argon atmosphere. About 2 g of $LiAlH_4$ mixed with 1, 3, 5, and 7 mol % $NiFe_2O_4$ nanoparticles was loaded in a sealed stainless-steel vial with a ZrO_2 milling ball-to-powder weight ratio of 20:1.

2.2. Characterization. The de/rehydrogenation behavior of the $LiAlH_4$ samples with and without $NiFe_2O_4$ catalyst was examined by using a Sieverts-type pressure−composition−temperature (PCT) equipment. The measurement is conducted in a reactor, which consists of two parts, heater and sample vessel, and the limiting conditions of the PCT apparatus reach 10 MPa and 600 °C. The heater of the PCT apparatus is used to connect the pressure transducer and the thermocouple. It has a 2.2 cm outside diameter, 0.5 cm wall, and 20 cm internal length. The heater is loaded with the sample vessel with the 1 cm outside diameter, 0.1 cm wall, and 5 cm internal length.[20] During the measurement, the sample vessel was loaded with ∼0.4 g of $LiAlH_4$ doped with 1, 3, 5, and 7 mol % $NiFe_2O_4$ nanopowder upon heating to 250 °C at a heating rate of 4 °C/min under 0.1 atm H_2 pressure. During heating, the reactor loaded with the sample vessel is heated in the air furnace, and hydrogen released from the sample vessel first flows into the heater and then flows into the transit pressure transducer, which can record the level of hydrogen pressure. The dehydrogenation amounts, calculated for all samples, were converted to pure $LiAlH_4$ with the elimination of various impurities.

The thermal decomposition behavior of $LiAlH_4$ with and without $NiFe_2O_4$ catalyst was measured by using a Netzsch model 449C differential scanning calorimeter (DSC) at heating rates of 6, 9, and 12 °C/min between 35 and 300 °C under a flow of 50 mL/min high-purity argon atmosphere, respectively.

FTIR analyses of all samples at room temperature were carried out by using a Bruker Vector 22 FTIR spectrometer. Scans were performed between 750 and 2000 cm^{-1} with a spectral resolution of 4 cm^{-1}.

The morphology of the samples has been analyzed by scanning electron microscopy (SEM, ZEISS EVO 18, Germany). During the sample preparation for the SEM measurements, the handling was conducted inside the glovebox. The prepared sample was moved to the SEM chamber to decrease the effect of moisture and oxidation on the testing results.

The XRD spectra of the sample before and after de/rehydrogenation were recorded by using an XRD (MXP21VAHF) with Cu Kα radiation between 10 and 90°, 0.02° per step.

3. RESULTS AND DISCUSSION

3.1. Dehydrogenation Properties Analysis. *3.1.1. Nonisothermal Dehydrogenation Properties.* The thermal desorption performance of the as-received $LiAlH_4$, as-milled $LiAlH_4$, and $LiAlH_4$ samples with 1, 3, 5, and 7 mol % $NiFe_2O_4$ nanoparticles is shown in Figure 1. As seen in Figure 1, without

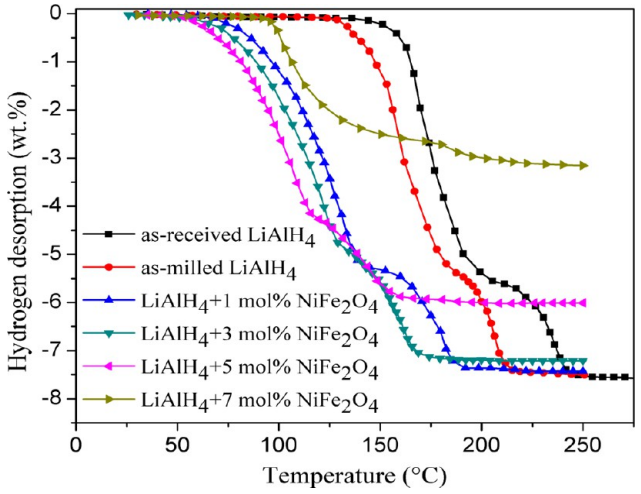

Figure 1. Thermal desorption profiles of the as-received $LiAlH_4$, as-milled $LiAlH_4$, and $LiAlH_4$ doped with 1, 3, 5, and 7 mol % $NiFe_2O_4$ nanopowder. The samples were heated to 250 °C at 4 °C/min heating rate.

adding $NiFe_2O_4$ nanopowder, the desorption curves of pure $LiAlH_4$ samples before and after ball milling exhibit the typical two-stage dehydrogenation reactions R1 and R2. It is clear that the decomposition of the as-received $LiAlH_4$ occurs at around 155 and 200 °C for the first two dehydrogenation processes, followed by 5.0 and 2.5 wt % released hydrogen, respectively. Thus, the sum amount of hydrogen released for the as-received $LiAlH_4$ reaches up to 7.5 wt % below 250 °C. While compared with the as-received $LiAlH_4$, the onset desorption temperatures for the as-milled $LiAlH_4$ both decrease by 21 °C at the first two

dx.doi.org/10.1021/jp408364p | J. Phys. Chem. C 2013, 117, 25917−25925

dehydrogenation steps, attributed to the decrease in $LiAlH_4$ grain size by mechanical milling.[8,23,26,29,31] After doping the $NiFe_2O_4$ nanoparticles into the $LiAlH_4$ matrix, the dehydrogenation process for the $LiAlH_4$+1 mol % $NiFe_2O_4$ sample starts at 68 °C. With increasing the $NiFe_2O_4$ proportion to 3 mol %, the onset decomposition temperature further decreases to 61 °C, which shows a 94 °C decrease, compared with that of the as-received $LiAlH_4$. Meanwhile, during the first two dehydrogenation processes, the total amount of H_2 released from 1 and 3 mol % $NiFe_2O_4$-doped $LiAlH_4$ is 7.4 and 7.2 wt %, respectively, close to the amount of hydrogen released from pristine $LiAlH_4$. By increasing the additive amount to 5 mol %, the dehydrogenation process further diminishes to 58 °C, showing a significant decline between the as-received $LiAlH_4$ and the 5 mol % doped sample in the onset dehydrogenation temperature. Meanwhile, hydrogen released for the $LiAlH_4$+5 mol % $NiFe_2O_4$ sample drops to 5.9 wt % at the first two dehydrogenation stages, which reveals that doping $NiFe_2O_4$ nanopowders into $LiAlH_4$ can significantly decline the onset desorption temperature of $LiAlH_4$. It is worthwhile to note that with further addition of 7 mol % $NiFe_2O_4$ the dehydrogenation process initiates at 100 °C, which is much higher than that for the $LiAlH_4$ sample containing fewer $NiFe_2O_4$ nanopowders. This abnormal phenomenon could be explained by merely 3.2 wt % hydrogen released for the $LiAlH_4$+7 mol % $NiFe_2O_4$ sample, which only accounts for 42.7% of pure $LiAlH_4$ and demonstrates the completion of the first dehydrogenation step (reaction R1) for the $LiAlH_4$+7 mol % $NiFe_2O_4$ sample during the milling process. Thus, the significant reduction in hydrogen capacity could result from the low onset dehydrogenation temperature of $LiAlH_4$+7 mol % $NiFe_2O_4$ sample compared with the samples doped with less $NiFe_2O_4$ content, resulting in hydrogen released during the ball-milling process. On the basis of the above nonisothermal hydrogen desorption analysis, it can be concluded that an excess amount of $NiFe_2O_4$ addition could significantly reduce the onset desorption temperature but leads to a remarkable loss of hydrogen release at the same time. Moreover, the initial desorption temperature of $LiAlH_4$ remarkably decreased to 58 °C by doping 5 mol % $NiFe_2O_4$ nanopowders, which is quite lower than that of $LiAlH_4$ with the addition of other various previously reported catalysts.[4,5,17−20,24,26,30,31] Meanwhile, combining these two considerations from the initial dehydrogenation temperature and hydrogen release capability, the optimal content of $NiFe_2O_4$ additive of the doped sample with the best dehydrogenation performance is 3 mol %, and the $LiAlH_4$+3 mol % $NiFe_2O_4$ sample will be utilized for analyzing the catalytic effect and mechanism of $NiFe_2O_4$ in the following tests. Although $NiFe_2O_4$ nanopowder has exhibited superior catalytic performance by declining the onset dehydrogenation temperature of $LiAlH_4$, the reversibility of the completely dehydrogenated 3 mol % doped sample cannot be tested at 140 °C under 6.5 MPa hydrogen pressure, as shown in Figure S1 (Supporting Information), resulting from the thermodynamic properties of $LiAlH_4$.[24]

3.1.2. Isothermal Dehydrogenation Properties. To further exhibit the remarkable catalytic effect of the $NiFe_2O_4$ nanopowder on the dehydrogenation properties of $LiAlH_4$, we employed the isothermal measurement to test the dehydriding kinetics of $LiAlH_4$. The isothermal dehydrogenation curves of the $LiAlH_4$+3 mol % $NiFe_2O_4$ sample heated at 90, 120, and 150 °C are shown in Figure 2. Moreover, Figure 2a,b also exhibits the dehydriding kinetics of the as-received and the as-milled $LiAlH_4$ heated at 120 °C to compare the dehydriding kinetics of undoped and doped samples. As seen in Figure 2, the desorption rates of pure $LiAlH_4$ before and after ball milling are dreadfully sluggish at 120 °C, and only 0.7 and 0.8 wt % of hydrogen were detected within 180 min, respectively, demonstrating the perishing desorption kinetics of pristine $LiAlH_4$. However, compared with the pure $LiAlH_4$, the desorption kinetics of $LiAlH_4$ is greatly enhanced after doping Ni ferrite nanopowders. For the $LiAlH_4$+3 mol % $NiFe_2O_4$ sample, ~4.9 wt % hydrogen was released at 90 °C in 160 min, which suggests the completion of the first dehydrogenation step (reaction R1). When the 3 mol % doped sample was heated to 120 °C, 7.0 wt % of hydrogen was released within 91 min, 6.3 wt % larger than that of pristine Li alanate for the same conditions. Furthermore, the first two dehydrogenation stages require only 30 min to finish with further increasing the heating temperature to 150 °C. Therefore, the $NiFe_2O_4$-doped sample exhibits superiority in improving $LiAlH_4$ desorption kinetics compared with $LiAlH_4$ sample doped with numerous previously documented catalysts.[4,21−27,29,30] Meanwhile, the ascendant desorption kinetics coupled to such a large quantity of hydrogen released at a moderate operating temperature makes practical sense for the proton exchange membrane (PEM) fuel cell applications.

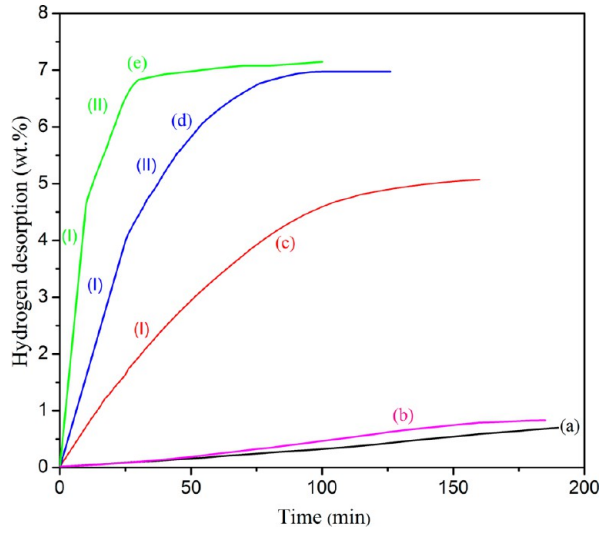

Figure 2. Isothermal desorption kinetics of (a) as-received, (b) as-milled $LiAlH_4$ at 120 °C, and $LiAlH_4$+3 mol % $NiFe_2O_4$ sample at (c) 90, (d) 120, and (e) 150 °C. (I) represents the first dehydrogenation stage; (II) represents the second dehydrogenation stage.

3.2. Thermal Analysis. DSC analysis was utilized to further specify the remarkable catalytic effect of Ni ferrite nanopowder on the dehydrogenation behavior of $LiAlH_4$. Figure 3 presents the DSC plot of the as-received $LiAlH_4$ and the $LiAlH_4$+3 mol % $NiFe_2O_4$ sample at various heating rates of 6, 9, and 12 °C/min between 35 and 300 °C, respectively. For the DSC curve of the as-received $LiAlH_4$, there are two endothermic peaks and two exothermic peaks, as seen in Figure 3a. The first and the second exothermic peaks correspond to the interaction between $LiAlH_4$ and surface hydroxyl impurities[36] and the decomposition of liquid $LiAlH_4$, respectively. Meanwhile, the two endothermic peaks reflect $LiAlH_4$ melting[36] and Li_3AlH_6 decomposition,[17] respectively. As for the $NiFe_2O_4$-doped $LiAlH_4$ sample, the exo/endothermic reactions can be seen in Figure 3b. All exothermic peaks of the 3 mol % $NiFe_2O_4$-doped

dx.doi.org/10.1021/jp408364p | J. Phys. Chem. C 2013, 117, 25917−25925

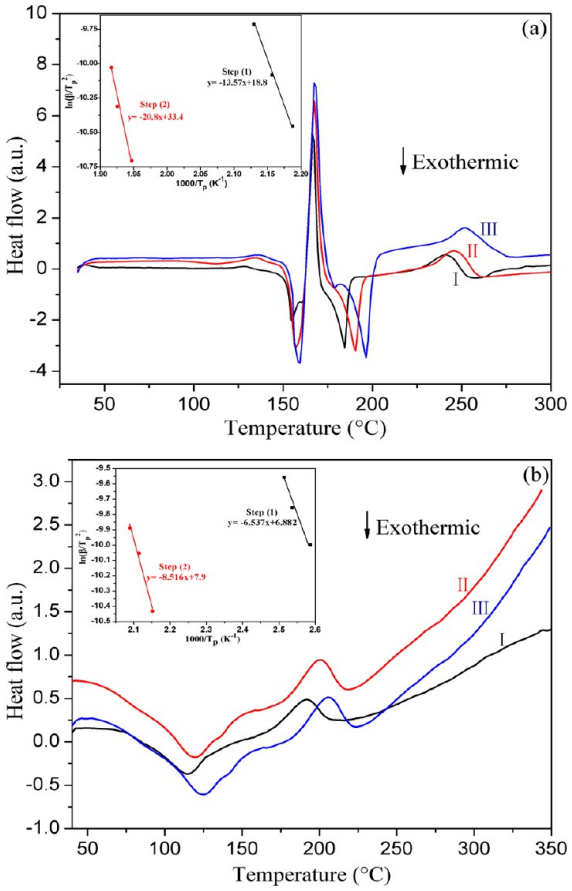

Figure 3. DSC profiles of (a) as-received $LiAlH_4$ and (b) $LiAlH_4$+3 mol % $NiFe_2O_4$ and the corresponding heating rates are (I) 6 °C/min, (II) 9 °C/min, and (III) 12 °C/min, respectively. The inset graphs show the Kissinger plots for the first two decomposition steps of (a) as-received $LiAlH_4$ and (b) $LiAlH_4$+3 mol % $NiFe_2O_4$.

sample appear below 125 °C, implying that the decomposition of $LiAlH_4$ occurs prior to its melting, so the two peaks correspond to the decomposition process of solid-state $LiAlH_4$ and Li_3AlH_6, respectively. The resulting peak temperatures in Figure 3b are lower than those of $LiAlH_4$ doped with various catalysts documented in recent reports.[16,24,26,29−31] In addition, the onset desorption temperatures have a discrepancy between PTC and DSC measurements for the same tested sample. This phenomenon could be explained by the different heating rate coupled to the different decomposition atmospheres during DSC measurement under 1 atm Ar and PCT measurement under 0.1 atm H_2, resulting in the different driving force for the desorption process of $LiAlH_4$ doped with $NiFe_2O_4$ nanopowder.[24]

The apparent activation energy (E_a) of the undoped and doped samples for the first two decomposition stages was calculated using the Kissinger method:[37]

$$\frac{\mathrm{d}\ln\left(\frac{\beta}{T_p^2}\right)}{\mathrm{d}\left(\frac{1}{T_p}\right)} = -\frac{E_a}{R} \quad (1)$$

where β is the heating rate, T_p expresses the peak temperature, and R is the gas constant. According to the slope of these lines in the inset graphs of Figure 3, the values of E_a of the as-received $LiAlH_4$ for the first two decomposition reactions are 114.3 and 172.6 kJ/mol. Nevertheless, the values of E_a for the $LiAlH_4$+3 mol % $NiFe_2O_4$ sample are calculated to be 54.3 and 70.8 kJ/mol, which are 73.6 and 101.8 kJ/mol lower than those of the as-received $LiAlH_4$ for the first two dehydrogenation reactions, respectively, suggesting that the dehydrogenation kinetics of $LiAlH_4$ obtained a significant improvement by doping $NiFe_2O_4$ nanoparticles. Table 1 shows the comparison of E_a for $LiAlH_4$ before and after doping to further emphasize the catalytic effect of $NiFe_2O_4$ nanopowder on dehydrogenation of $LiAlH_4$. By comparing the decline rate of E_a of the $NiFe_2O_4$-doped sample with other catalysts-doped samples, the decline rate of E_a of $LiAlH_4$ doped with $NiFe_2O_4$ is 52.5% for the first dehydrogenation stage. The second dehydrogenation stage has reached 59%, which indicates that the dehydrogenation properties of $LiAlH_4$ are evidently improved by the addition of $NiFe_2O_4$ nanoparticles compared with other reported catalysts. As a result, the activation energy barrier for the dehydrogenation of $LiAlH_4$ was effectively decreased by doping $NiFe_2O_4$ nanoparticles, resulting in the remarkable enhancement on the dehydrogenation performance of $LiAlH_4$.

3.3. Dehydrogenation Mechanism. Figure 4 shows the variation in particle size and powder morphology observed by SEM. As presented in Figure 4a, the as-received $LiAlH_4$ consists of large irregular polyhedron particles with an average size larger than 40 μm. However, the particles of $NiFe_2O_4$-doped sample present two features: first, the shape of the particles changes from irregular polyhedron to regular globular particles; second, the size of particles reduces to 2−10 μm, as seen in Figure 4b. Meanwhile, SEM images show that the embedded $NiFe_2O_4$ can be hardly observed in the $LiAlH_4$ matrix, resulting from their tiny original crystallite size (20 nm) and the interference of the $NiFe_2O_4$ particles magnetic properties with the SEM equipment.[31] Figure 4c−f provides the elemental maps, including aluminum, oxygen, iron, and nickel,

Table 1. Activation Energy (E_a) of $LiAlH_4$ Doped with Various Catalysts

	step 1			step 2			
	E_a (kJ/mol)			E_a (kJ/mol)			
nano catalysts	before doping	after doping	decline rate (%)	before doping	after doping	decline rate (%)	reference
TiO_2	114	49	57				29
Nb_2O_5	86	64.5	25	101	79	21.8	30
K_2TiF_6	116.2	78.2	32.7	133	90.8	31.7	26
$MnFe_2O_4$	111.6	66.7	40.2	180.7	75.8	58.1	31
TiC	86	59	31.4	101	70	30.7	16
n-Ni		~70			~100		8
$NiFe_2O_4$	114.3	54.3	52.5	172.6	70.8	59	this work

dx.doi.org/10.1021/jp408364p | J. Phys. Chem. C 2013, 117, 25917−25925

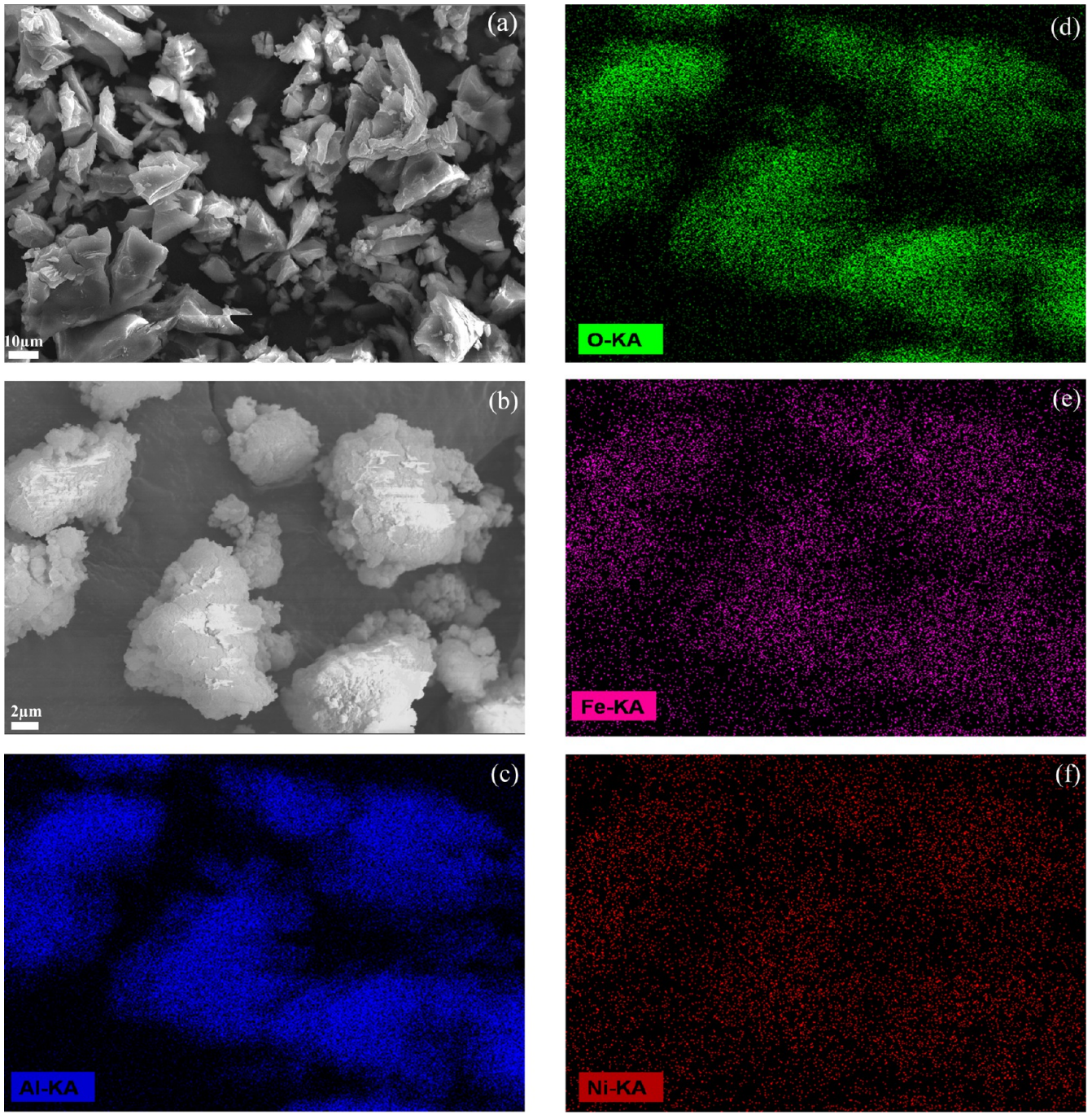

Figure 4. SEM images of (a) as-received $LiAlH_4$ and (b) $LiAlH_4$+3 mol % $NiFe_2O_4$ after ball milling with the corresponding element maps of the doped sample.

respectively, to better illustrate the elemental distribution of the $NiFe_2O_4$ catalyst around the $LiAlH_4$ particles. It can be concluded that all constituent elements of $NiFe_2O_4$ in the mixture are uniformly distributed around the surface of $LiAlH_4$ particles, which means that the Ni ferrite would be well mixed with $LiAlH_4$ after high-energy ball milling, and there exists a good contact between the catalyst and the $LiAlH_4$ particles. However, the elemental map of oxygen is more pronounced than that of iron and nickel, as seen in these two elemental maps, attributed to oxidation during the specimen preparation process. More crystal boundaries and high surface defects are introduced into the $LiAlH_4$ matrix due to the change in particles shape and the decrease in the particles size. Furthermore, the highly dispersed $NiFe_2O_4$ nanoparticles uniformly distributed around the surface of the $LiAlH_4$ matrix could serve as nucleation sites, contributing to lower the activation energy, and facilitate the dehydrogenation stages of pristine $LiAlH_4$. Therefore, the significant reduction in the crystallite size of the doped $LiAlH_4$ sample can introduce more grain boundaries and the high density of surface defects around the surface of $LiAlH_4$ matrix made by the dispersive catalyst properties, resulting in improved desorption properties.

In general, the mechanism for solid-state reactions can be determined by the kinetics rate equation, which classifies the reaction mechanisms into different models, listed in Table S1(Supporting Information), including diffusion, chemical

dx.doi.org/10.1021/jp408364p | J. Phys. Chem. C 2013, 117, 25917−25925

reaction, nuclei, nucleation, and so on.[5,16,30] To exactly specify the dehydrogenation reaction mechanism of $LiAlH_4$ doped with the $NiFe_2O_4$ nanoparticles, the rate equation of dehydrogenation kinetics was deduced, according to the experimental data of the isothermal dehydrogenation for the $LiAlH_4$+3 mol % doped sample heated at 90, 120, and 150 °C, as shown in Figure 5. Among these different dehydrogenation mechanism models, the most appropriate model will be chosen, giving larger linearity coefficient value and smaller residual sum of squares (RSS) among all models. Analyzing Figure 5a, the best linearity coefficient can be fitted by the F1 mechanism model formulated through the random nucleation approach, suggesting that nucleation process dominates the dehydrogenation of the $LiAlH_4$ doped with $NiFe_2O_4$ heated at 90 °C, and each active site has an equal probability to form nucleations.[38] It clearly illustrates that the desorption rates at different temperatures are controlled by different mechanisms, as shown in Figure 5b,c. Compared with the dehydrogenation process at 90 °C, the rate-limiting steps for diffusion are controlled by random nucleation mechanism at higher decomposition temperature. For the $NiFe_2O_4$-doped sample at 120 °C, the dehydrogenation process is found to comply with the reaction mechanism corresponding to the A2 model, as shown in Figure 5b, indicating that the random nucleation process appears in the mixture, and the nucleation growth is dominated by the 2-D growth deduced from the Avrami–Erofeev equation. As a result, the dehydrogenation reaction follows an interface reaction with constant interface velocity.[30,38] It is evident that there exists minor difference in the correlation coefficient value among the F1, R2, and R3 models in Figure 5c upon desorption at 150 °C, but the RSS of R2 shows more superiority than the other two models. Thus, it is noticeable that R2 (R^2 > 0.99, RSS < 0.05) gives a better fit than R3 and F1 kinetics models upon desorption at 150 °C. Analyzing the mechanism of R2 model, it can be concluded that the dispersed $NiFe_2O_4$ nanoparticles could form a thin layer transformed phase in the $LiAlH_4$ matrix surface, resulting in introducing large amounts of nucleation sites on the surface of $LiAlH_4$ particles to facilitate the dehydrogenation products generation. Furthermore, the dehydrogenation kinetics is mainly dominated by the interface movement of the dehydrided phases along the 2-D network from the particle surface into the bulk.[30] In summary, at higher isothermal dehydrogenation temperature, the diffusion limitations would dominate over random nucleation for the 3 mol % $NiFe_2O_4$-doped sample.

To investigate the effect of addition of nanosized nickel ferrite on the $LiAlH_4$ vibrational spectrum, we provide the FTIR spectra of the as-milled $LiAlH_4$ and 1, 3, and 7 mol % $NiFe_2O_4$–$LiAlH_4$ composites after ball milling with scanning range from 750 to 2000 cm^{-1} in Figure 6. $LiAlH_4$ contains two kinds of Al–H bonds in the active infrared vibration, corresponding to Al–H stretching modes (1600–1800 cm^{-1}) and Li–Al–H bending modes (800–900 cm^{-1}).[16,26,31,35] With regard to the Li_3AlH_6, there is only one kind of the Al–H stretching modes (1500–1400 cm^{-1}) in the active infrared vibration.[39] As seen in Figure 6, for the 1 and 3 mol %

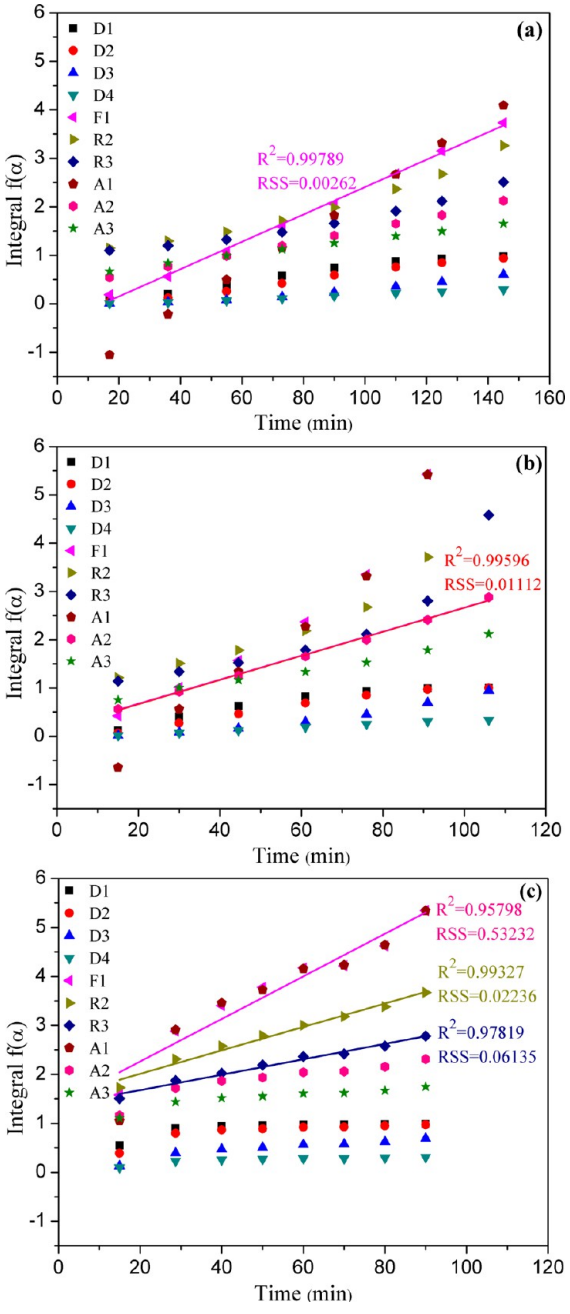

Figure 5. Curves of different kinetic models applied to the isothermal dehydrogenation of $LiAlH_4$+3 mol % $NiFe_2O_4$ at (a) 90, (b) 120, and (c) 150 °C.

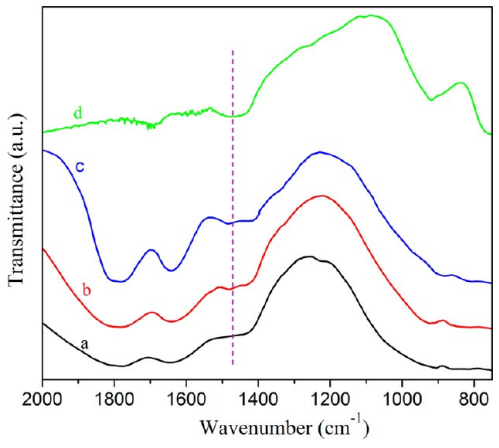

Figure 6. FTIR spectra of (a) as-milled $LiAlH_4$, (b) 1 mol %, (c) 3 mol %, and (d) 7 mol % $NiFe_2O_4$-doped $LiAlH_4$ after ball milling.

dx.doi.org/10.1021/jp408364p | J. Phys. Chem. C 2013, 117, 25917–25925

$NiFe_2O_4$-doped samples, all IR absorption peaks corresponding to $LiAlH_4$ still exist, while the IR absorption peak of Li_3AlH_6 appears at 1471 cm^{-1} compared with the IR absorption spectra of the as-milled $LiAlH_4$. Furthermore, the intensity of the IR absorption peak of Li_3AlH_6 at 1471 cm^{-1} continuously fortifies with enhancing the $NiFe_2O_4$ proportion from 1 to 3 mol %, suggesting that the doped $LiAlH_4$ decomposes to a larger extent and hydrogen is released during mechanical ball milling. On the contrary, there is no IR absorption peak of Li_3AlH_6 appearing in the IR absorption spectra of the as-milled $LiAlH_4$ in Figure 6 (curve a). Also, for the 7 mol % $NiFe_2O_4$–$LiAlH_4$ composite, the IR absorption peak of $LiAlH_4$ cannot be observed. As a result, the 7 mol % doped sample completely decomposed and generated the dehydrogenation product of Li_3AlH_6 during the mechanical ball milling, which has been proven by the dehydriding capacity of the 7 mol % doped $LiAlH_4$ (Figure 1). From the detailed FTIR analysis, the 7 mol % $NiFe_2O_4$–$LiAlH_4$ sample fully decomposed during the ball milling and formed Li_3AlH_6, which could be further validated by the following XRD measurements.

Figure 7 shows the XRD spectra of the as-milled $LiAlH_4$ and the 1, 3, and 7 mol % $NiFe_2O_4$-doped $LiAlH_4$ samples after ball

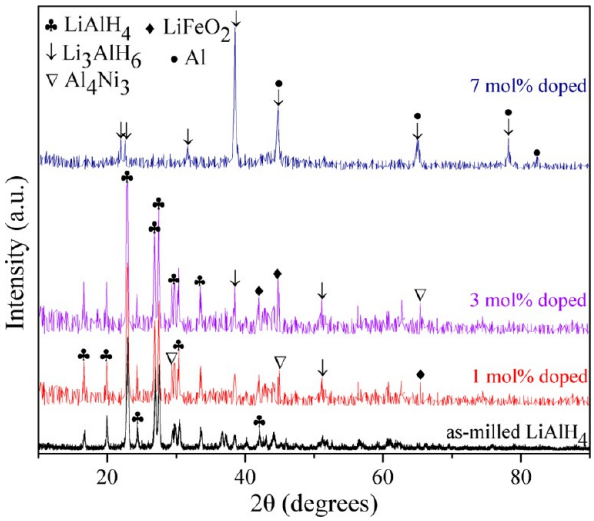

Figure 7. XRD patterns of as-milled $LiAlH_4$ and 1, 3, and 7 mol % $NiFe_2O_4$-doped $LiAlH_4$ samples after ball milling.

milling. With regard to the diffraction data of the as-milled $LiAlH_4$ sample, there are only $LiAlH_4$ diffraction peaks without any diffraction peaks corresponding to the decomposition products, except for the small amount of an unknown impurity, indicating that pure $LiAlH_4$ did not decompose during ball milling.[9,24,26,29] However, for the $NiFe_2O_4$-doped samples, the detection results demonstrate that these samples are not physical mixtures of $LiAlH_4$ and nickel ferrite, and there is an existing amount of the decomposition products. For the 1 mol % doped sample after mechanical ball milling, these weak diffraction peaks, corresponding to Li_3AlH_6 and microcrystalline Al, were detected. Meanwhile, the diffraction peaks of $LiFeO_2$ were observed at 34.8, 41.3, and 44.7°; the diffraction peaks of Al_4Ni_3 were found at 29.3, 44.9, and 65.4°, signifying the reaction between $LiAlH_4$ and $NiFe_2O_4$, which occurred during ball milling. Consequently, the dopant phase cannot be detected in the XRD pattern for those samples after ball milling. As for the $LiAlH_4$+3 mol % $NiFe_2O_4$ sample, the diffraction peaks exhibit the decomposition products, including $LiFeO_2$, Al_4Ni_3, Al, and Li_3AlH_6, and the diffraction intensity of these dehydrogenation products was enhanced compared with the 1 mol % doped sample. However, the $LiAlH_4$ peak intensity declined, signifying that $LiAlH_4$ reacted with $NiFe_2O_4$ and more $LiAlH_4$ decomposed during ball milling. Surprisingly, with regard to the $LiAlH_4$+7 mol % $NiFe_2O_4$ sample, $LiAlH_4$ peaks cannot be observed, and all of the diffraction peaks correspond to the following decomposition products: $LiFeO_2$, Al_4Ni_3, Al, and Li_3AlH_6. A similar phenomenon is also found in the reported literature results for TiF_3-[23] and $MnFe_2O_4$-[31] doped $LiAlH_4$ samples. It is assumed that the $LiAlH_4$ peak disappearance in the 7 mol % sample is due to the reaction occurring between $LiAlH_4$ and $NiFe_2O_4$, and the sample complete decomposition during the ball milling. Meanwhile, the $NiFe_2O_4$ nanophases cannot be detected in the XRD patterns of all doped samples, mainly because the complete reaction occurred between $LiAlH_4$ and $NiFe_2O_4$, forming $LiFeO_2$, Al_4Ni_3, Al, and Li_3AlH_6 phases. In the previous literature reports, similar phenomenon was observed for $NiCl_2$-,[22] TiF_3-,[23] NbF_5-,[24] TiO_2-,[29] and $MnFe_2O_4$[31]-doped $LiAlH_4$ as additives, which also could not be detected after ball milling. Attracted by the low onset desorption temperature, some ball-milling methods will be utilized for the purpose of preventing $LiAlH_4$ decomposition during the mechanical ball milling.

For elucidating the phase transitions of these samples during the dehydrogenation process, XRD measurements on the as-milled $LiAlH_4$ and $LiAlH_4$+1, 3, and 7 mol % $NiFe_2O_4$ samples after desorption at 250 °C are present in Figure 8. Diffraction

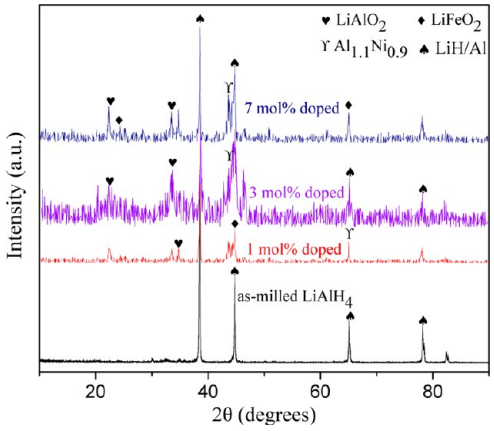

Figure 8. XRD patterns of as-milled $LiAlH_4$ and 1, 3, and 7 mol % $NiFe_2O_4$-doped $LiAlH_4$ samples after the first two dehydrogenation stages.

patterns of the as-milled $LiAlH_4$ after dehydrogenation show that there are LiH and Al phases existing as the dehydrogenation products. The XRD patterns of the $NiFe_2O_4$-doped samples show that there are not only LiH and Al phases but also $LiFeO_2$, $LiAlO_2$, and $Al_{1.1}Ni_{0.9}$ phases as the dehydrogenation products, which is quite different from the as-milled samples. With the increasing $NiFe_2O_4$ amount, the $LiFeO_2$ and $Al_{1.1}Ni_{0.9}$ peaks gradually strengthen. These in situ formed reaction products may act as catalysts during the dehydrogenation process of $LiAlH_4$. Meanwhile, the reactions occurred during the dehydrogenation process could enhance the dehydrogenation dynamics of $LiAlH_4$. These favorable factors contributed to the significantly improved dehydrogenation properties of $LiAlH_4$.

dx.doi.org/10.1021/jp408364p | J. Phys. Chem. C 2013, 117, 25917−25925

From the above analyses, the significantly improved dehydrogenation properties of $LiAlH_4$ by doping $NiFe_2O_4$ nanopowder could be explained by the following reasons. First, a great number of reaction nucleation sites and hydrogen diffusion channels were introduced, resulting from reducing the particle size and creating numerous defects in the $LiAlH_4$ matrix during the dehydrogenation process. Second, $NiFe_2O_4$ reacted with $LiAlH_4$, leading to form Li−Fe oxide ($LiFeO_2$) and Al−Ni compound (Al_4Ni_3) during mechanical ball milling. Then, the $LiFeO_2$, $LiAlO_2$, and $Al_{1.1}Ni_{0.9}$ phases appeared as the dehydrogenation products in the XRD patterns, and the diffraction peaks of these products gradually strengthen with further increasing the additive amount. It is believed that these finely dispersed reaction products generated during the high-energy ball-milling process act as real catalysts to promote the decomposition of $LiAlH_4$ by serving as the active sites for nucleation and growth of the dehydrogenation products. Third, a series of reactions between $LiAlH_4$ and $NiFe_2O_4$ occurred during heating. It is expected that these reactions can alter the thermodynamics by decreasing the decomposition enthalpy. As a result, it is believed that refinement of the $LiAlH_4$ powder combined with the reactions between $LiAlH_4$ and $NiFe_2O_4$ together contribute to the significantly enhanced dehydrogenation performance of $LiAlH_4$.

4. CONCLUSIONS

In summary, the dehydrogenation performance of nanosized $NiFe_2O_4$-doped $LiAlH_4$ samples has been significantly improved compared with the neat Li Alanate powder. Compared with the as-received $LiAlH_4$, the onset desorption temperature of the $LiAlH_4$+3 mol % $NiFe_2O_4$ sample decreased to 94 and 72 °C for the first two decomposition steps, respectively, followed with ∼7.2 wt % hydrogen released. On the basis of the isothermal dehydriding kinetics analysis, the 3 mol % doped sample can desorb about 7.0 wt % of hydrogen within 91 min under 0.1 MPa pressure at 120 °C, which is 6.3 wt % higher than that of the pristine $LiAlH_4$ under the same experimental conditions. From the DSC and Kissinger analyses, a 52.5 and 59% decline in E_a for the first two dehydrogenation stages of $LiAlH_4$ can be obtained, showing the maximum for $LiAlH_4$ doped with other various previously documented catalysts. On the basis of the FTIR and XRD analyses of the undoped and doped samples, a series of reactions occurred between $LiAlH_4$ and $NiFe_2O_4$ during ball milling and formed $LiFeO_2$ and Al_4Ni_3 as the decomposition products. Moreover, reactions proceed during the heating process and $LiFeO_2$, $LiAlO_2$, and Al_4Ni_3 were produced. These in situ-formed decomposition products, coupled to the reactions produce a synergistic influence on remarkably enhancing the dehydrogenation properties of $LiAlH_4$. Hence, $NiFe_2O_4$ is an effective catalyst for significantly improving the dehydrogenation performance of $LiAlH_4$.

■ ASSOCIATED CONTENT

Supporting Information

The result of the rehydrogenation of $LiAlH_4$+3 mol % $NiFe_2O_4$ sample at 140 °C under 6.5 MPa H_2 for 2.5 h. Kinetic models examined for the isothermal dehydrogenation curves of $NiFe_2O_4$-doped $LiAlH_4$ at 90, 120, and 150 °C. This material is available free of charge via the Internet at http://pubs.acs.org.

■ AUTHOR INFORMATION

Corresponding Author

*E-mail: quxh@ustb.edu.cn (X.Q.). Tel: +86-10-62332700. Fax: +86-10-62334311.

Notes

The authors declare no competing financial interest.

■ ACKNOWLEDGMENTS

We thank the National High-Tech R&D Program (863 Program) of China (2006AA05Z132) for financial support of this research. F.Z. thanks China Scholarship Council (CSC) for providing the scholarship.

■ REFERENCES

(1) Zheng, X. P.; Xiao, G.; Ma, Q. H.; Liu, S. L.; Li, T.; Feng, X.; Zheng, J. J. Hydrogen Release Capacity of the $LiAlH_4$-MgH_2 System. *J. Power Sources* **2013**, *231*, 173−176.

(2) Wan, Q.; Li, P.; Li, Z. L.; Zhao, K. F.; Liu, Z. W.; Zhai, F. Q.; Qu, X. H.; Volinsky, A. A. $NaAlH_4$ Dehydrogenation Properties Enhanced by $MnFe_2O_4$ Nanoparticles. *J. Power Sources* **2014**, *248*, 388−395.

(3) Bogdanovic, B.; Schwickardi, M. Ti-Doped Alkali Metal Aluminium Hydrides as Potential Novel Reversible Hydrogen Storage Materials. *J. Alloys Compd.* **1997**, *253*, 1−9.

(4) Li, L.; Qiu, F. Y.; Wang, Y. J.; Xu, Y. A.; An, C. H.; Liu, G.; Jiao, L. F.; Yuan, H. T. Enhanced Hydrogen Storage Properties of TiN-$LiAlH_4$ Composite. *Int. J. Hydrogen Energy* **2013**, *38*, 3695−3701.

(5) Li, L. G.; Gu, Q. F.; Tang, Z. W.; Chen, X. W.; Tan, Y. B.; Li, Q.; Yu, X. B. Two Novel Derivatives of Ammonia Borane for Hydrogen Storage: Synthesis, Structure, and Hydrogen Desorption Investigation. *J. Mater. Chem. A* **2013**, *1*, 12263−12269.

(6) Andreasen, A.; Veggea, T.; Pedersena, A. S. Dehydrogenation Kinetics of As-Received and Ball-Milled $LiAlH_4$. *J. Solid State Chem.* **2005**, *178*, 3672−3678.

(7) Resan, M.; Hampton, M. D.; Lomness, J. K.; Slattery, D. K. Effects of Various Catalysts on Hydrogen Release and Uptake Characteristics of $LiAlH_4$. *Int. J. Hydrogen Energy* **2005**, *30*, 1413−1416.

(8) Varin, R. A.; Zbroniec, L. The Effects of Nanometric Nickel (n-Ni) Catalyst on the Dehydrogenation and Rehydrogenation Behavior of Ball Milled Lithium Alanate ($LiAlH_4$). *J. Alloys Compd.* **2010**, *506*, 928−939.

(9) Zheng, X. P.; Li, P.; An, F. Q.; Wang, G. Q.; Qu, X. H. Effects of Ti and Fe Additives on Hydrogen Release from Lithium Alanate. *Rare Met. Mater. Eng.* **2008**, *37*, 400−403.

(10) Balema, V. P.; Wiench, J. W.; Dennis, K. W.; Pruski, M.; Pecharsky, V. K. Titanium Catalyzed Solid-State Transformations in $LiAlH_4$ during High-Energy Ball-Milling. *J. Alloys Compd.* **2001**, *329*, 108−114.

(11) Chen, J.; Kuriyama, N.; Xu, Q.; Takeshita, H. T.; Sakai, T. Reversible Hydrogen Storage via Titanium-Catalyzed $LiAlH_4$ and Li_3AlH_6. *J. Phys. Chem. B* **2001**, *105*, 11214−11220.

(12) Langmi, H. W.; McGrady, G. S.; Liu, X. F.; Jensen, C. M. Modification of the H_2 Desorption Properties of $LiAlH_4$ through Doping with Ti. *J. Phys. Chem. C* **2010**, *114*, 10666−10669.

(13) Schlapbach, L.; Zuttel, A. Hydrogen-Storage Materials for Mobile Applications. *Nature* **2001**, *414*, 353−358.

(14) Mehraj-ud-din, N.; Sami-ullah, R.; So, C. S.; Hwang, S. W.; Kim, A. R.; Nahm, K. S. Thermal Decomposition of $LiAlH_4$ Chemically Mixed with Lithium Amide and Transition Metal Chlorides. *Int. J. Hydrogen Energy* **2009**, *34*, 8937−8943.

(15) Hima, K. L.; Viswanathan, B.; Srinivasa, M. S. Dehydriding Behaviour of $LiAlH_4$−the Catalytic Role of Carbon Nanofibres. *Int. J. Hydrogen Energy* **2008**, *33*, 366−373.

(16) Rafi-ud-din; Zhang, L.; Li, P.; Qu, X. H. Catalytic Effects of Nano-Sized TiC Additions on the Hydrogen Storage Properties of $LiAlH_4$. *J. Alloys Compd.* **2010**, *508*, 119−128.

(17) Andreasen, A. Effect of Ti-doping on the Dehydrogenation Kinetic Parameters of Lithium Aluminum Hydride. *J. Alloys Compd.* **2006**, *419*, 40−44.
(18) Ares Fernandez, J. R.; Aguey-Zinsou, K. F.; Elsaesser, M.; Ma, X. Z.; Dornheim, M.; Klassen, T.; Bormann, R. Mechanical and Thermal Decomposition of $LiAlH_4$ with Metal Halides. *Int. J. Hydrogen Energy* **2007**, *32*, 1033−1040.
(19) Suttisawat, Y.; Rangsunvigit, P.; Kitiyanana, B.; Muangsinb, N.; Kulprathipanjac, S. Catalytic Effect of Zr and Hf on Hydrogen Desorption/Absorption of $NaAlH_4$ and $LiAlH_4$. *Int. J. Hydrogen Energy* **2007**, *32*, 1277−1285.
(20) Zheng, X. P.; Li, P.; Humail, I. S.; An, F. Q.; Wang, G. Q.; Qu, X. H. Effect of Catalyst $LaCl_3$ on Hydrogen Storage Properties of Lithium Alanate ($LiAlH_4$). *Int. J. Hydrogen Energy* **2007**, *32*, 4957−4960.
(21) Kojima, Y.; Kawai, Y.; Matsumoto, M.; Haga, T. Hydrogen Release of Catalyzed Lithium Aluminum Hydride by a Mechanochemical Reaction. *J. Alloys Compd.* **2008**, *462*, 275−278.
(22) Sun, T.; Huang, C. K.; Wang, H.; Sun, L. X.; Zhu, M. The Effect of Doping $NiCl_2$ on the Dehydrogenation Properties of $LiAlH_4$. *Int. J. Hydrogen Energy* **2008**, *33*, 6216−6221.
(23) Liu, S. S.; Sun, L. X.; Zhang, Y.; Xu, F.; Zhang, J.; Chu, H. L.; Fan, M. Q.; Zhang, T.; Song, X. Y.; Grolier, J. P. Effect of Ball Milling Time on the Hydrogen Storage Properties of TiF_3-Doped $LiAlH_4$. *Int. J. Hydrogen Energy* **2009**, *34*, 8079−8085.
(24) Ismail, M.; Zhao, Y.; Yu, X. B.; Dou, S. X. Effects of NbF_5 Addition on the Hydrogen Storage Properties of $LiAlH_4$. *Int. J. Hydrogen Energy* **2010**, *35*, 2361−2367.
(25) Varin, R. A.; Zbroniec, L. Fast and Slow Dehydrogenation of Ball Milled Lithium Alanate ($LiAlH_4$) Catalyzed with Manganese Chloride ($MnCl_2$) as Compared to Nanometric Nickel Catalyst. *J. Alloys Compd.* **2011**, *509S*, S736−S739.
(26) Li, Z. B.; Liu, S. S.; Si, X. L.; Zhang, J.; Jiao, C. L.; Wang, S.; Liu, S.; Zou, Y. J.; Sun, L. X.; Xu, F. Significantly Improved Dehydrogenation of $LiAlH_4$ Destabilized by K_2TiF_6. *Int. J. Hydrogen Energy* **2012**, *37*, 3261−3267.
(27) Fu, J.; Röntzsch, L.; Schmidt, T.; Tegel, M.; Weißgärber, T.; Kieback, B. Comparative Study on the Dehydrogenation Properties of $TiCl_4$-Doped $LiAlH_4$ Using Different Doping Techniques. *Int. J. Hydrogen Energy* **2012**, *37*, 13387−13392.
(28) Zheng, X. P.; Zheng, J. J.; Ma, Q. H.; Liu, S. L.; Feng, X.; Lin, X. B.; Xiao, G. Study on Dehydrogenation Properties of the $LiAlH_4$-NH_4Cl System. *J. Alloys Compd.* **2013**, *551*, 508−511.
(29) Ismail, M.; Zhao, Y.; Yu, X. B.; Nevirkovets, I. P.; Dou, S. X. Significantly Improved Dehydrogenation of $LiAlH_4$ Catalysed with TiO_2 Nanopowder. *Int. J. Hydrogen Energy* **2011**, *36*, 8327−8334.
(30) Rafi-ud-din.; Qu, X. H.; Li, P.; Zhang, L.; Ahmad, M. Hydrogen Sorption Improvement of $LiAlH_4$ Catalyzed by Nb_2O_5 and Cr_2O_3 Nanoparticles. *J. Phys. Chem. C* **2011**, *115*, 13088−13099.
(31) Zhai, F. Q.; Li, P.; Sun, A. Z.; Wu, S.; Wan, Q.; Zhang, W. N.; Li, Y. L.; Cui, L. Q.; Qu, X. H. Significantly Improved Dehydrogenation of $LiAlH_4$ Destabilized by $MnFe_2O_4$ Nanoparticles. *J. Phys. Chem. C* **2012**, *116*, 11939−11945.
(32) Li, Z. L.; Li, P.; Wan, Q.; Zhai, F. Q.; Liu, Z. W.; Zhao, K. F.; Wang, L.; Lü, S. Y.; Zou, L.; Qu, X. H.; et al. Dehydrogenation Improvement of $LiAlH_4$ Catalyzed by Fe_2O_3 and Co_2O_3 Nanoparticles. *J. Phys. Chem. C* **2013**, *117*, 18343−18352.
(33) Liu, S. S.; Li, Z. B.; Jiao, C. L.; Si, X. L.; Yang, L. N.; Zhang, J.; Zhou, H. Y.; Huang, F. L.; Gabelica, Z.; Schick, C.; et al. Improved Reversible Hydrogen Storage of $LiAlH_4$ by Nano-Sized TiH_2. *Int. J. Hydrogen Energy* **2013**, *38*, 2770−2777.
(34) Zheng, X. P.; Liu, S. L. Study on Hydrogen Storage Properties of $LiAlH_4$. *J. Alloys Compd.* **2009**, *481*, 761−763.
(35) Ismail, M.; Zhao, Y.; Yu, X. B.; Ranjbar, A.; Dou, S. X. Improved Hydrogen Desorption in Lithium Alanate by Addition of SWCNT-Metallic Catalyst Composite. *Int. J. Hydrogen Energy* **2011**, *36*, 3593−3599.
(36) McCarty, M.; Maycock, J. N.; Verneker, V. R. P. Thermal Decomposition of Lithium Aluminum Hydride. *J. Phys. Chem.* **1968**, *72*, 4009−4014.
(37) Kissinger, H. E. Reaction Kinetics in Differential Thermal Analysis. *Anal. Chem.* **1957**, *29*, 1702−1706.
(38) Mahfouz, R. M.; Al-Shehri, S. M.; Monshi, M. A. S.; El-salam, A. B. D. Isothermal Decomposition of γ-Irradiated Dysprosium Acetate. *Radiat. Eff. Defects Solids* **2002**, *157*, 515−519.
(39) Liu, S. S.; Zhang, Y.; Sun, L. X.; Zhang, J.; Zhao, J. N.; Xu, F.; Huang, F. L. The Dehydrogenation Performance and Reaction Mechanisms of Li_3AlH_6 with TiF_3 Additive. *Int. J. Hydrogen Energy* **2010**, *35*, 4554−4561.